An Integrated Model Validation Study of the Wave Front Tip/Tilt System Using the Micro-Precision Interferometer Testbed

Ipek Basdogan
ipek.basdogan@jpl.nasa.gov
(818) 354-0952

Frank Dekens
frank.g.dekens@jpl.nasa.gov
(818) 354-7652

Gregory W. Neat
neat@huey.jpl.nasa.gov
(818) 354-0584

Jet Propulsion Laboratory,
California Institute of Technology
4800 Oak Grove Drive
Pasadena, CA 91109

structural modeling
optical modeling
pointing control
model validation

Abstract– This paper presents a validation study of a specific integrated modeling methodology which is a candidate tool for modeling complex opto-mechanical systems such as spaceborne interferometers. The methodology integrates structural, optical, and control system modeling into a common environment: the Integrated Modeling of Optical Systems (IMOS) software package. This study is one of many from a planned sequence that uses the Micro-Precision Interferometer (MPI) testbed, which is a ground-based, full-scale hardware model of a spaceborne interferometer. Parallel development of the MPI testbed and an IMOS model of MPI enabled a unique opportunity to validate the modeling methodology with actual measurements from the test article. This particular study assesses the ability of the MPI IMOS model to predict the performance of the MPI wave front tip/tilt system. The current validation was done in the open loop optics, hard mounted disturbance configuration. Results demonstrate MPI IMOS model predictions that are within a factor of 3 of the testbed measurements.

TABLE OF CONTENTS

1. INTRODUCTION

Detection of earth-like planets around stars by measuring the stars motion requires an instrument with micro-arcsecond astrometric measurement accuracy [1]. Spaceborne optical interferometers are likely to be the first instrument class capable of achieving this accuracy level. Interferometry is a technique in which the light from two collecting apertures are combined in order to achieve the equivalent resolution of a single telescope with a diameter equal to the separation distance of the two collecting apertures. When the light is combined properly it interferes and this can be detected in the form of an interference fringe. The resulting data, the fringe amplitudes, phases and positions, may be used to produce an image of the observed object or to measure the angular separation of multiple objects. For the Space Interferometry Mission (SIM), the instrument requires stabilization of the optical path lengths, where each optical path travels through one of the collecting apertures, to be equal down to the nanometer level, as well as laser metrology measurements of path length changes down to the tens of picometer [2]. The charter of JPL's Interferometer Technology Program (ITP) is to mitigate risk for this optical interferometer mission [3]. A number of ongoing complementary activities address these technological challenges. These activities are: integrated modeling methodology development and validation, metrology and vibration attenuation hardware testbed development, and flight qualification of the interferometer components. Among these activities, the integrated modeling will be used in the spacecraft and instrument design to reduce the mission risks. This paper investigates the ability of the integrated modeling methodology to meet these demanding analysis needs.

In anticipation of these needs, the Integrated Modeling of Optical Systems (IMOS) and the Controlled Optics Modeling Package (COMP) software packages were developed at JPL [4,5]. The integrated modeling methodology combines structural, optical, and control system design within a common software environment which enables an end-to-end performance evaluation of the system requirements. Coincident with this development, the Micro-Precision Interferometer (MPI) testbed was built to assess vibration attenuation technologies on a dynamically and dimensionally representative hardware model of the spaceborne interferometer (see Figure1) [6].

An integrated model of MPI was developed in parallel with the testbed. This modeling/hardware synergy resulted in a

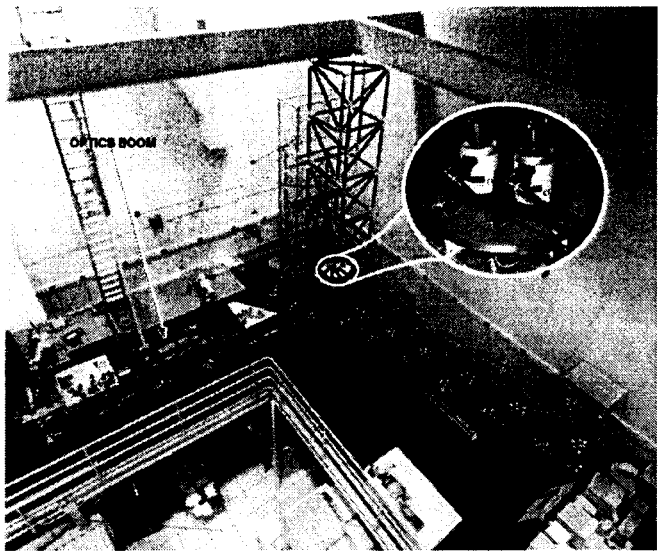

Figure 1 Bird's-eye view of the MPI Testbed (Hard mounted disturbance configuration in the zoomed area).

unique opportunity to validate the modeling methodology by comparing model predictions with the testbed measurements. If SIM adopts the IMOS modeling strategy, the error bars which quantify the difference between the actual measurement and the model prediction on MPI will ultimately be applied to the future SIM models. This will allow a confidence level to be associated with a given SIM design that was created using a model for which the prediction accuracy is known.

Fundamental interferometer operation requires that the two independent telescopes view the same star. The wave front tip/tilt system, or the pointing control system, is responsible for providing this function. This system adjusts four degrees of freedom: tip and tilt of the two incoming beams. The fringe tracking system stabilizes the optical path difference (OPD) between the two telescopes or equivalently the stellar fringe position. All previous MPI validation studies involved the performance prediction of the fringe tracking subsystem. This has been done for the open loop, hard mounted configuration for a number of models, each with a different fidelity [7]. In addition, the modeling methodology has been validated for the closed loop, hard mounted configuration using the high fidelity model [8].

This paper presents the validation of the wave front tilt system predicted by the high fidelity model in the open loop optics, hard mounted disturbance configuration. This system, for the same measurement, has four times as many degrees of freedom as the fringe tracking system. Since each telescope is effectively an independent pointing system, each interferometer arm can be validated independently, and we will concentrate on one of these arms, which is referred as the inboard arm in the Section 4. The goal for this study is to achieve a prediction accuracy of 2 which was the accuracy level achieved for the analogous OPD validation using this model [8].

2. WAVE FRONT TIP/TILT VALIDATION PROCEDURE

Figure 2 presents the integrated modeling methodology validation procedure for the wave front tip/tilt system.

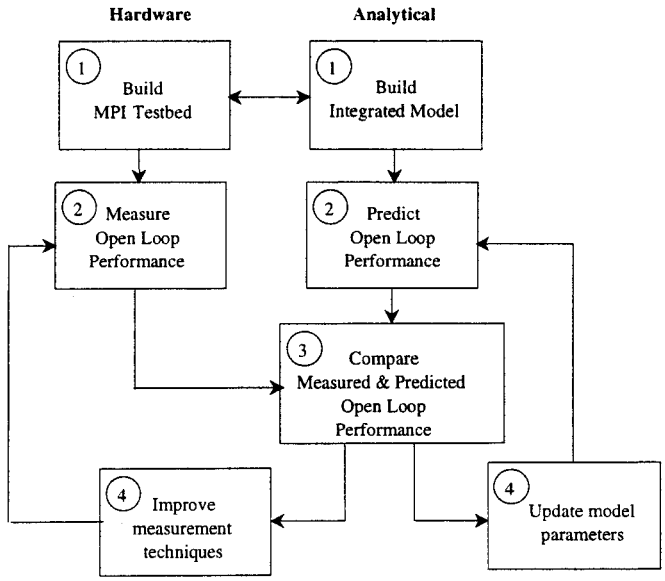

Figure 2 Integrated modeling methodology validation procedure for the open loop optics, hard mounted disturbance case.

The figure depicts each step as either a hardware or an analysis procedure. The first step is the parallel process of building the testbed and the simulation model. This process has been a continuous effort during the development of the MPI testbed from a simple structure to a full-scale interferometer. For our ongoing study, this step involves updating the optical and structural model based on the new configuration of MPI testbed for the wave front tip/tilt analysis. Step 2 involves measuring and predicting the disturbance input to wave front tip/tilt output transfer functions for the testbed and model respectively. The details of the analytical model and measurement techniques will be explained in Sections 3 and 5 respectively. Step 3 represents the comparison of the model predictions with the testbed measurements using a metric based on output power. Finally, step 4 represents the improvements/adjustments made to the testbed/model based on the comparison.

3. MPI INTEGRATED MODEL

The MPI integrated model consists of a structural finite element model and a linear optical model integrated together. The structural model is generated with IMOS, whereas both IMOS and COMP are used to create the optical model. The integration and disturbance analysis are performed in MATLAB with the aid of IMOS functions.

3.1 Structural Model

The structural model is specified in IMOS as a finite element geometry, shown in Figure 3. This geometry

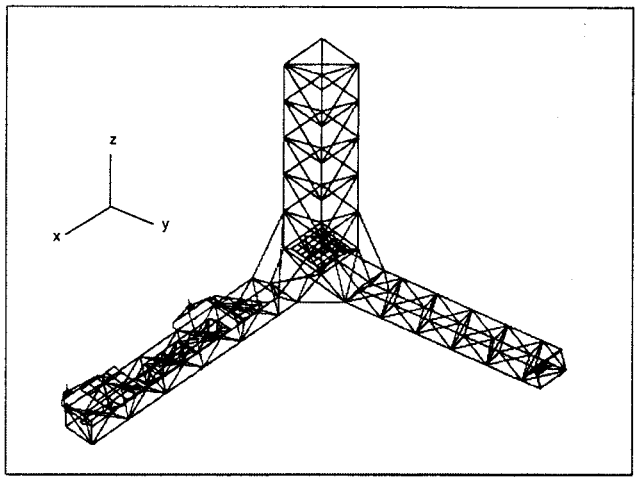

Figure 3 MPI finite element geometry

consists of plate, beam, truss, and rigid body elements, modeling the base truss structure and the components. The base truss structure is made up of three booms: a horizontal optics boom (along the *x-axis*), a vertical tower (along the *z-axis*), and a canted metrology boom (along the *y-axis*). The components consist of inboard and outboard optics plates, a disturbance mount plate, two siderostat mounts, an optics cart containing an active delay line, the optics cart support structure, a passive delay line, and an external metrology beam launcher plate. The finite element model uses 3,094 degrees of freedom (dof) of which 2,158 dofs are independent with respect to multi-point constraints of the rigid body elements [4].

The governing equation for the multiple degree of freedom system generated by the finite element analysis is

$$\mathbf{M}\ddot{\mathbf{d}} + \mathbf{C}\dot{\mathbf{d}} + \mathbf{K}\mathbf{d} = \mathbf{F}\mathbf{u} \tag{1}$$

where **M** and **K** are the mass and stiffness matrices of the system. The vector **d** is the nodal displacements, **u** is the control input and **F** is the influence matrix for **u**. Assuming proportional damping where the damping matrix is proportional to the mass and stiffness matrix, the matrix **C** takes the form

$$\mathbf{C} = \alpha\mathbf{M} + \beta\mathbf{K} \tag{2}$$

where α and β are constants. The nodal displacement vector can be expressed in terms of the modal coordinates by using the mode shapes of the undamped system as

$$\mathbf{d} = \Phi\eta \tag{3}$$

where Φ is the modal transformation matrix and η is the vector of modal coordinates. Substituting Eq. 3 into Eq. 1 and premultiplying this equation by Φ^T yields

$$\mathbf{M}_P\ddot{\eta} + \mathbf{C}_P\dot{\eta} + \mathbf{K}_P\eta = \mathbf{F}_P\mathbf{u} \tag{4}$$

where

$$\begin{aligned} \mathbf{M}_P &= \Phi^T\mathbf{M}\Phi, \\ \mathbf{C}_P &= \Phi^T\mathbf{C}\Phi, \\ \mathbf{K}_P &= \Phi^T\mathbf{K}\Phi, \\ \mathbf{F}_P &= \Phi^T\mathbf{F}. \end{aligned} \tag{5}$$

Equation 4 can then be rewritten as n uncoupled differential equations as

$$\ddot{\eta}_i + 2\zeta_i\omega_i\eta_i + \omega_i^2\eta_i = f_i \qquad i = 1,2,...,n \tag{6}$$

where ζ_i is the modal damping factor, and ω_i is the natural frequency of mode *i*. The modal damping factor ζ_i is assumed to be %0.3 for the global flexible-body modes and %3 for the dynamics associated with the delay line structure. These damping values are consistent with the estimates obtained from the modal tests [9].

3.2 Optical Model

The optical model begins with a specification of the optical prescription. This prescription includes the shapes, positions, and orientations of the optical elements. A ray trace of the optical prescription is shown in Figure 4. Note that Figure 4 indicates the location of the pointing control system actuator: fast steering mirror (FSM) and the sensor: camera (CCD). This optical prescription together with the structural model is generated in IMOS based on the layout of the actual optical elements on MPI. Optical model generation uses the structural finite element geometry in order to simplify prescription definition and to ease the succeeding structural-optical model integration. This allows the location of optical elements to be measured with respect to reference points on the structure as opposed to with each other. Furthermore, structural nodes that correspond to optical element attachment points are easily identified or defined.

Once the optical prescriptions are specified, they are exported to COMP, where linear optical models are created. These linear models are calculated by performing an analytic differential ray trace [5]. The result is a model of the form:

$$\mathbf{y} = \mathbf{C}_{opt}\,\mathbf{d}_{opt} \tag{7}$$

where $\mathbf{d}_{opt}$ is a vector of optical element perturbations (*i.e.*, a subset of **d** in Eq. 1), **y** is a vector of optical output, and $\mathbf{C}_{opt}$ is the optical sensitivity matrix giving the change in ray state due to perturbations of the optical elements. The optical output can be pathlength difference, wave front tip/tilt, or beam sheer depending on the analysis performed.

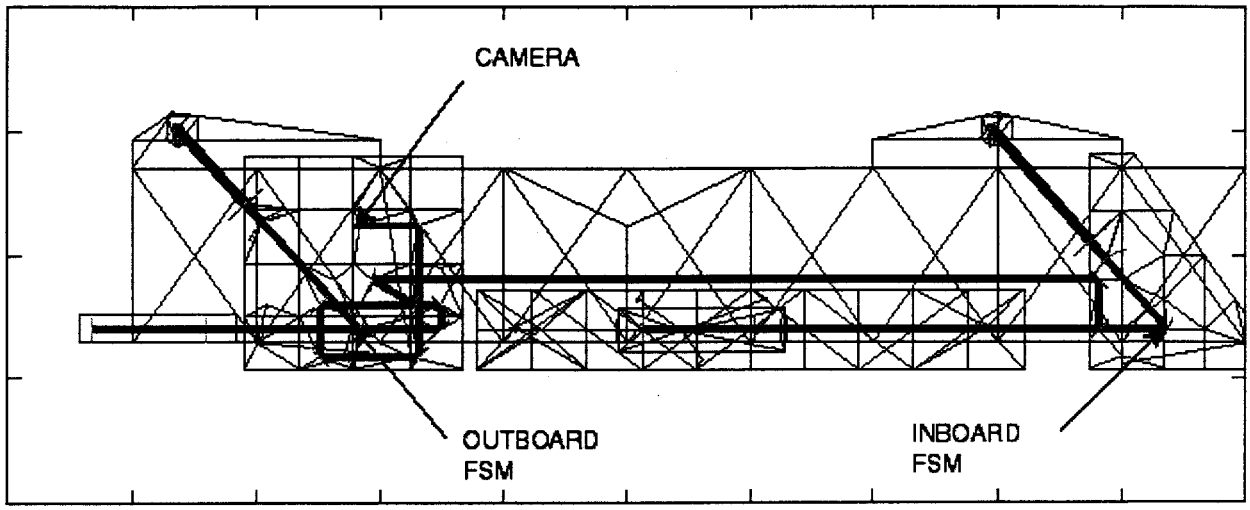

Figure 4 Ray trace of the MPI optical prescription on the finite element geometry of the optics boom.

3.3 Structural-Optical Model Integration

Once the structural and optical models have been created, they are integrated to form a structural-optical model. This integrated model is specified in first-order, state-space form, lending itself most easily to analysis and control synthesis with existing MATLAB functions.

First, the structural model is truncated to remove modes above the bandwidth of expected disturbances (*i.e.* above 950 Hz) [10]. The truncated modal model is then converted into first-order, state-space form by using the substitution

$$\mathbf{x} = \begin{bmatrix} \eta_k \\ \dot{\eta}_k \end{bmatrix} \tag{8}$$

where the subscript k refers to the set of kept mode shapes.

Resulting in:

$$\begin{aligned} \dot{\mathbf{x}} &= \mathbf{A}\mathbf{x} + \mathbf{B}\mathbf{u} \\ \mathbf{d} &= \mathbf{C}_d\,\mathbf{x} \end{aligned} \tag{9}$$

with:

$$\mathbf{A} = \begin{bmatrix} \mathbf{0} & \mathbf{I} \\ -\mathbf{M}_P^{-1}\mathbf{K}_P & -\mathbf{M}_P^{-1}\mathbf{C}_P \end{bmatrix}$$

$$\mathbf{B} = \begin{bmatrix} 0 \\ \mathbf{M}_P^{-1}\mathbf{F}_P \end{bmatrix} \qquad [\mathbf{C}_d] = [\Phi \quad \mathbf{0}] \tag{10}$$

Finally, the linear optical model is incorporated. The optical output is obtained by premultiplying **d** by a zero-padded optical sensitivity matrix, $\tilde{\mathbf{C}}_{opt}$. This matrix is simply $\mathbf{C}_{opt}$ with zero columns added corresponding to elements of **d** that are not connected to optical elements (i.e., that are not in $\mathbf{d}_{opt}$). In this case the **C** matrix for the state space model becomes:

$$\mathbf{C} = \tilde{\mathbf{C}}_{opt}\,\mathbf{C}_d \tag{11}$$

and yields to a state space model in the form of

$$\begin{aligned} \dot{\mathbf{x}} &= \mathbf{A}\mathbf{x} + \mathbf{B}\mathbf{u} \\ \mathbf{y} &= \mathbf{C}\mathbf{x} \end{aligned} \tag{12}$$

Taking the Laplace transform on both sides of Eq.12 yields

$$s\mathbf{X}(s) - \mathbf{x}(0) = \mathbf{A}\mathbf{X}(s) + \mathbf{B}\mathbf{U}(s) \tag{13a}$$

$$\mathbf{Y}(s) = \mathbf{C}\mathbf{X}(s) \tag{13b}$$

where $\mathbf{X}(s) = L[\mathbf{x}(t)]$ and $\mathbf{U}(s) = L[\mathbf{u}(t)]$, and L is the Laplace transform operator [11]. Here we drop the initial condition vector $\mathbf{x}(0)$ since the dynamic characteristics of linear systems are independent of the initial conditions. By collecting common terms, Eq. 13a becomes

$$\mathbf{X}(s) = (s\mathbf{I} - \mathbf{A})^{-1}\mathbf{B}\mathbf{U}(s) \tag{14}$$

Substitution of Eq.14 into Eq. 13b results in

$$\mathbf{Y}(s) = [\mathbf{C}(s\mathbf{I} - \mathbf{A})^{-1}\mathbf{B}]\mathbf{U}(s) = \mathbf{H}(s)\mathbf{U}(s) \tag{15}$$

where $\mathbf{H}(s)$ is the transfer function that relates the output $\mathbf{Y}(s)$ to the given input $\mathbf{U}(s)$

$$\mathbf{H}(s) = \frac{\mathbf{Y}(s)}{\mathbf{U}(s)} \tag{16}$$

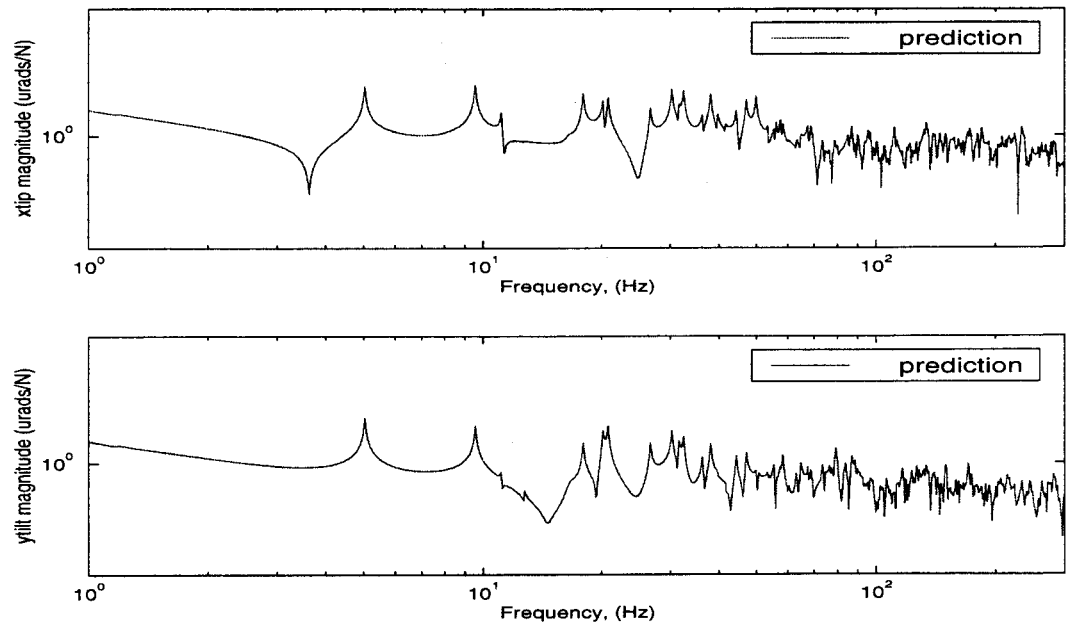

Figure 5 Predicted *x-axis* force input disturbance to wave front tip/tilt output transfer functions.

Figure 5 shows the transfer function for the x-axis disturbance input to wave front tip/tilt output. These transfer functions are obtained using the standard MATLAB functions after the state space model is built.

4. MPI OPTICAL LAYOUT

Figure 6 is a schematic of the MPI optics boom and traces the optical path from the artificial star through the testbed's optical train. The artificial star is a commercial heterodyne laser that sits on a pneumatically supported optical table. The beam is split by a polarizing beamsplitter (PBS) and each side is expanded to a 50 mm beam. A number of fold mirrors direct the beams to the two interferometer arms on the suspended MPI structure. The light path taken by the right hand beam is described below, and the other path is similar. We refer to the right and left hand sides of the interferometer as the inboard and outboard beams respectively. The siderostat is the first optical element on the air suspended structure. A subsequent beam compressor is used to reduce the input beam diameter from 50 mm to 30 mm to obtain an output beam suitable for traversing the delay line optics with sufficient light for the fringe-tracking sensor. Next comes a fast steering mirror which is used for pointing control. Three piezo actuators position the mirror, providing tip and tilt motion for the closed-loop configuration. After traveling through the active delayline and a couple of folding mirrors, the inboard beam is reflected on a 50% beam splitter. Here the reflected light joins the transmitted beam from the outboard path. After the beam combiner, the central portion of the combined stellar beams passes through the hole in an annular pick-off mirror to a fringe detector. The annular pick off mirror and subsequent folding mirrors reflects the outer annulus of each beam towards a high speed CCD camera. The 32 by 32 pixel CCD camera is the sensor for the pointing control subsystem. The two beams are focused, by a 1 meter focal length lens, at different positions on the CCD camera by a wedge angle introduced into the outboard arm. This is accomplished by inserting an annular glass wedge between the delay line and folding flat. This wedge has a matching central hole to that of the annular pick-off mirror, such that, only the portion of the beam that is used for tip/tilt sensing has the extra tilt, while the central portion of the two beams will stay parallel and interfere properly. The tilt between the two beams allows the pointing of each beam to be sensed with a single detector.

5. MPI DISTURBANCE TRANSFER FUNCTION MEASUREMENT

In this study, disturbance input to wave front tip/tilt output transfer functions are measured since they completely characterize (in a linear sense) the propagation of disturbances to wave front tip/tilt. Figure 7 shows the disturbance input location and the camera output location on the MPI testbed. A pair of 10 N shakers mounted on a custom 6-axis force measuring device (dynamometer) are used for the disturbance source. The output is the centroid position on the camera for the inboard beam. An 11 by 11 pixel window on the camera, which is centered on its initial diffraction pattern location is sampled at 1000 Hz. For each window, the first moment of the diffraction pattern is calculated, which we refer to as the centroid location. This is done in real time in order to measure the centroid motion and therefore beam tip and tilt. The offset from of the current centroid location to the reference centroid location is converted to two analog signals, namely the *xtip* and *ytilt* offsets on the CCD coordinate system. This can then be used as the output signal to a signal analyzer. An HP data analyzer is used to drive the shakers, record the dynamometer and centroid measurements and calculate the transfer function. The disturbance transfer functions were measured for three force disturbance directions: *x, y, z.*

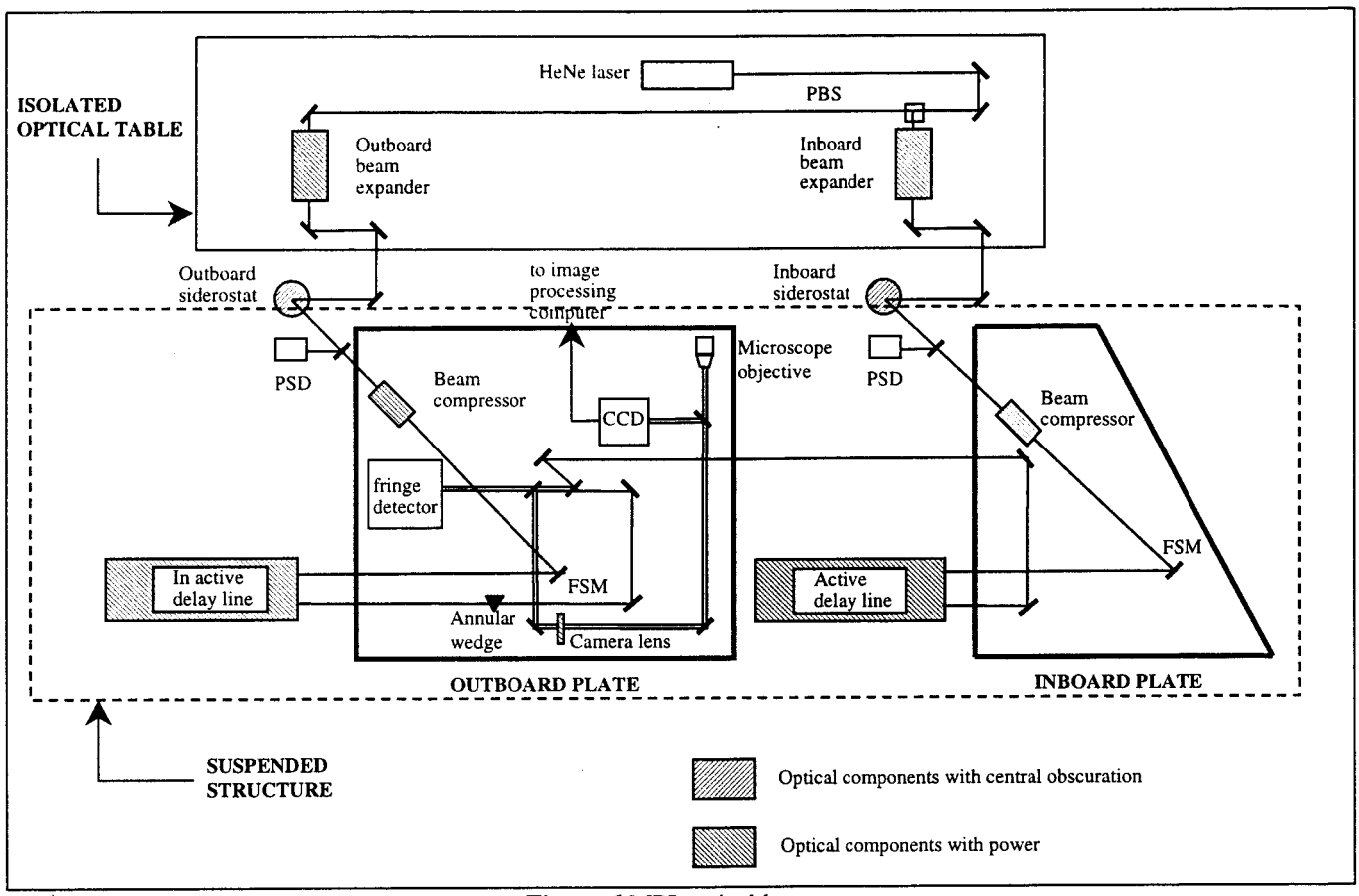

Figure 6 MPI optical layout.

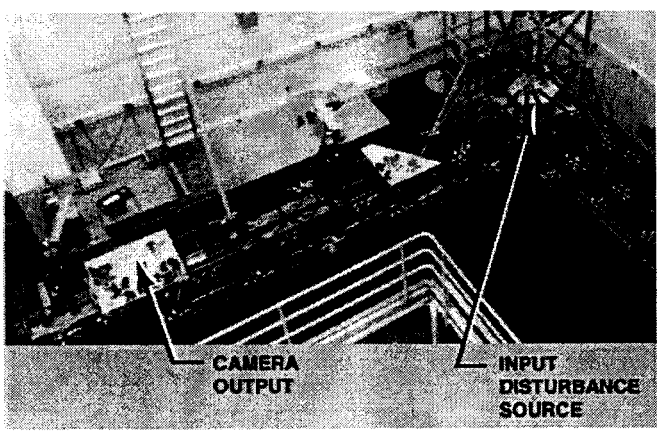

Figure 7 Locations of disturbance input and wave front tip/ tilt output on the MPI testbed.

6. RESULTS

The measured and predicted transfer functions are compared utilizing the metric that was developed for previous validation studies [9]. This metric, σ_g, is based on the variance of resulting WFT when the disturbance is band-limited white noise:

$$\sigma_g^2 = \frac{A_d}{\pi}\int_{fmin}^{fmax} \left|\mathbf{H}(j\omega)\right|^2 d\omega \qquad (17)$$

where A_d is the amplitude of the bandlimited white noise disturbance power spectral density, $\mathbf{H}(j\omega)$ is the transfer function from Eq. 16. The frequency range of interest is defined by f_{min} and f_{max}.

Using this metric, the accuracy of the model can be quantified by comparing σ_g for the predicted and measured transfer functions. The measured transfer functions, along with the corresponding predicted transfer functions, are shown in Figures 8-10.

The results of these comparisons are shown in Table 1. The table entries represent the ratio between the measured and predicted transfer functions for a number of bandwidths of interest between 4 -300 Hz. Below 4 Hz the force capability of the shakers are limited and the testbed suspension modes pollute the measurement. Above 300 Hz, MPI measurements are background noise limited. This bandwidth is broken down into decades for comparison purposes.

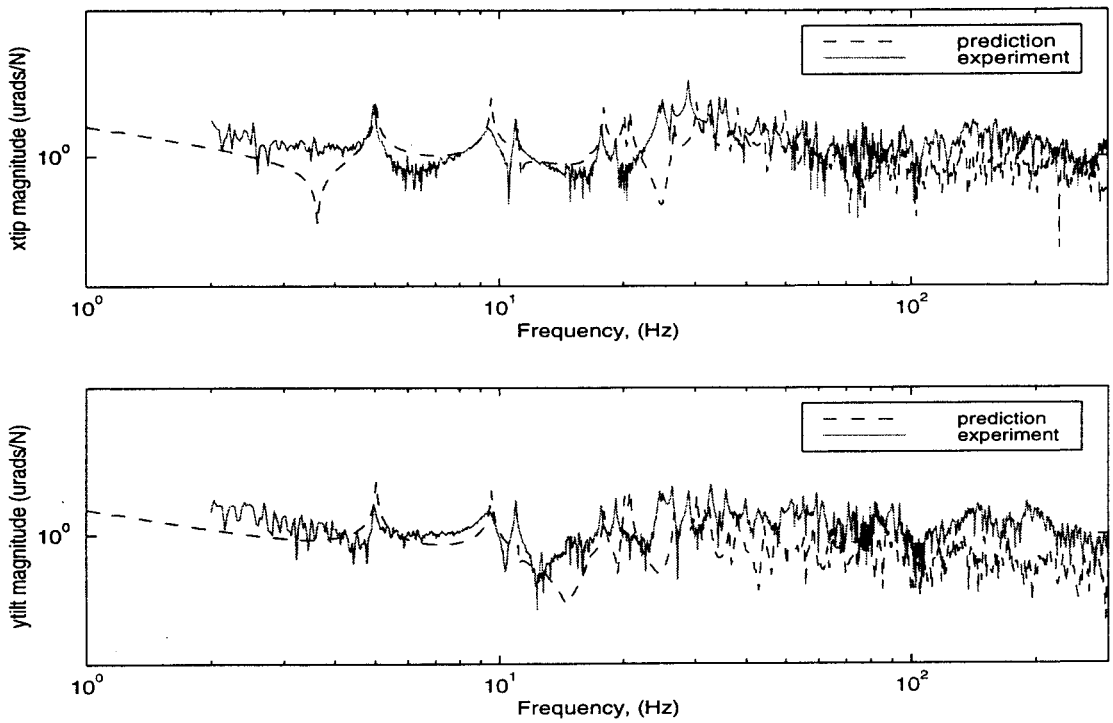

Figure 8 Predicted and measured *x-axis* force input disturbance to wave front tip/tilt output transfer functions.

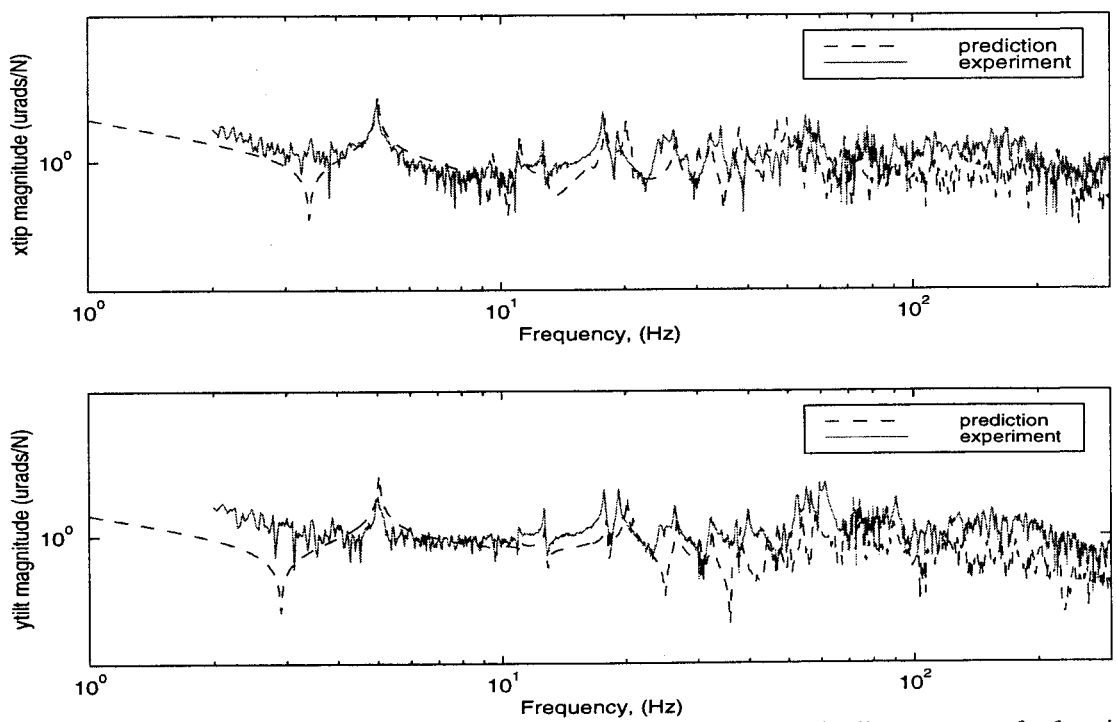

Figure 9 Predicted and measured *y-axis* force input disturbance to wave front tip/tilt output transfer functions.

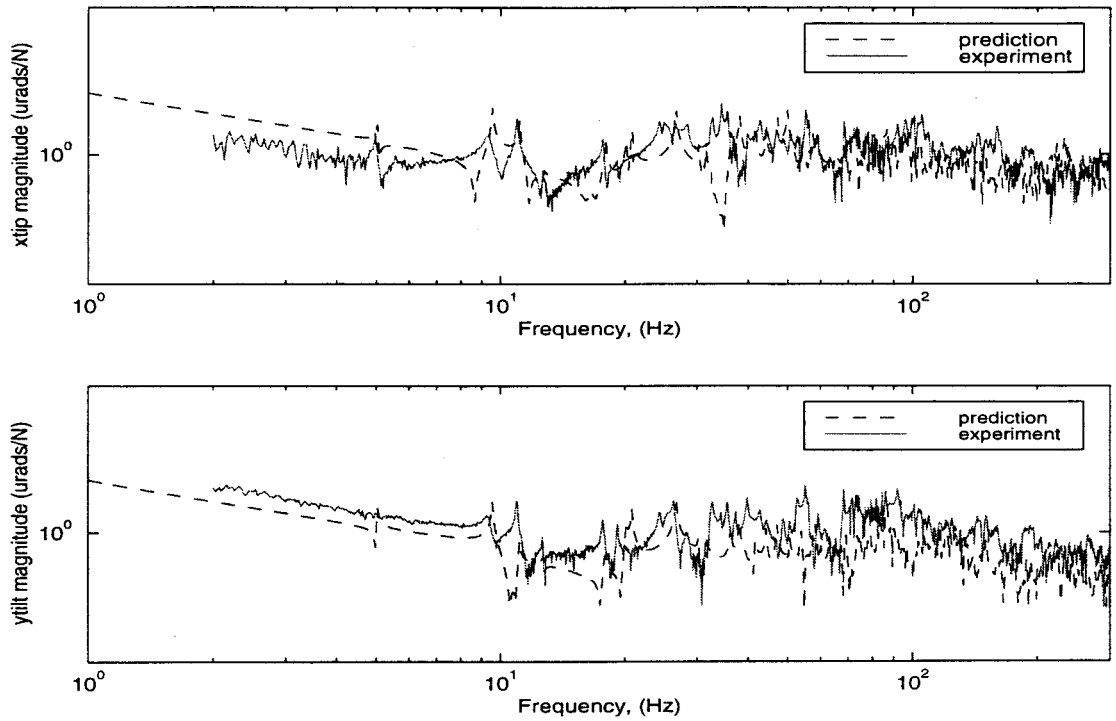

Figure 10 Predicted and measured *z-axis* force input disturbance to wave front tip/tilt output transfer functions.

Table 1 Metric comparison between the predicted and measured transfer functions for the MPI testbed.

Disturbance Input		σ_g predicted / σ_g measured			
		4-10 Hz	10-100 Hz	100-300 Hz	*4-300 Hz*
x-axis force	xtip	1.96	0.33	0.165	*0.35*
	ytilt	2.22	0.33	0.08	*0.33*
y-axis force	xtip	1.57	0.84	0.20	*0.77*
	ytilt	3.19	0.16	0.13	*0.30*
z-axis force	xtip	3.20	0.60	0.31	*0.55*
	ytilt	0.60	0.20	0.28	*0.22*

7. CONCLUSION

The integrated modeling methodology used to predict the wave front tip/tilt performance of a ground based interferometer testbed is presented. The high fidelity model used in this study includes an optical and a structural model integrated into a common software environment. The model predictions for the open loop, hard mounted disturbance configuration are validated utilizing the measured transfer functions. The validation procedure is based on a calculation which quantifies the differences between the analytical and experimental transfer functions across a number of bandwidths.

The current model predicts the wave front tilt variation performance within a factor of 3 for the broadband comparison between 4-300 Hz (see the last column of Table 1). Additional experimental and analytical improvements are being investigated. On the modeling side, these improvements include: detailed modeling of the optics mounts and updating the modal damping values based on the component studies. On the experimental side, these improvements include: improvements to the centroiding algorithm, reducing the ambient tip/tilt background and increasing the input force to the testbed.

In addition to the model and measurement improvements for this configuration, another area of future work involves adding torque input disturbances and the outboard interferometer output measurements the present validation study. Once the desired accuracy (factor of 2) is obtained, the disturbance isolator and the closed loop pointing control system will be incorporated into the integrated model to predict the wave front tilt performance for these configurations of the testbed.

The modeling effort and the MPI testbed have mutually benefited from the parallel effort and close coupling between the two. The proper validation techniques give us confidence in our modeling methodology and will allow us to place error bars on a future SIM IMOS models.

8. ACKNOWLEDGEMENTS

The work described in this paper was carried out at the Jet Propulsion Laboratory, California Institute of Technology, under contract with the National Aeronautics and Space Administration.

9. REFERENCES

[1] M. M. Colavita, M. Shao, and M. D. Rayman, "Orbiting stellar interferometer for astrometry and imaging," *Applied Optics*, vol. 32, no. 10, pp. 1789-1797, April 1993.

[2] M. Shao and D. M Wolf, "Orbiting stellar interferometer," *Proceedings of SPIE Symposium on Spaceborne Interferometry*, vol. 2447, (Orlando, FL), pp. 228-239, April 1995.

[3] R. A. Laskin, "Technology for space interferometry," *Proceedings of. 33rd Aerospace Sciences Meeting and Exhibit*, vol95-0825, (Reno,NV), AIAA, Jan 1995.

[4] M. H. Milman, H. C. Briggs, W. Ledeboer, J. W. Melody, R. L. Norton, and L. Needels, *Integrated Modeling of Optical Systems User's Manual, Release 2.0*, Nov. 1995. JPL D-13040.

[5] D. Redding, *Controlled Optics Modeling Package User Manual, Release 1.0*, June 1992. JPL D-9816.

[6] G. W. Neat, A. Abramovici, J. W. Melody, R. J. Calvet, N. M. Nerheim, and J. F. O'Brien, "Control technology readiness for spaceborne optical interferometer missions, " *Proceedings of Space Microdynamics and Accurate Control Symposium*, (Toulouse, France), May 1997.

[7] S. Joshi, J. W. Melody and G. W. Neat, "A case study of the role of structural/optical model fidelity in performance prediction of complex opto-mechanical instruments," *Proceedings of 36th IEEE Conference on Decision and Control*, (San Diego, CA), pp. 1367-1372, Dec 1997.

[8] J. W. Melody and G. W. Neat, "Integrated modeling methodology validation using the micro-precision interferometer testbed," *Proceedings of 35th IEEE Conference on Decision and Control*, vol. 4, (Kobe, Japan), pp. 4222-4227, Dec 1996.

[9] M. B. Levine-West and J. W. Melody, "Model updating of evolutionary structures," *Proceedings of 15th ASME Biennial Conference on Mechanical Vibration and Noise*, (Boston, MA), Sept. 1995.

[10] S. Shaklan, J. Yu, and H. C. Briggs, "Integrated structural and optical modeling of the orbiting stellar interferometer," *Proceedings of SPIE Symposium* on *Space Astronomical; Telescope and Instrument II*, (Orlando, FA), Apr. 1993.

[11] Y. W. Kwon and H. Bang, *The Finite Element Method using MATLAB*, CRC Press Inc., 1997.